Accumulated Lattice Strain as an Intrinsic Trigger for the First-Cycle Voltage Decay in Li-Rich 3d Layered Oxides

Suning Wang,△ Tian Zhao,△ Jinniu Chen, Alexander Missyul, Laura Simonelli, Laijun Liu, Fujun Li, Xiangyang Kong, and Weibo Hua*

ABSTRACT: Li- and Mn-rich layered oxides (LMLOs) are promising cathode materials for Li-ion batteries (LIBs) owing to their high discharge capacity of above 250 mA h g^{-1}. A high voltage plateau related to the oxidation of lattice oxygen appears upon the first charge, but it cannot be recovered during discharge, resulting in the so-called voltage decay. Disappearance of the honeycomb superstructure of the layered structure at a slow C-rate (e.g., 0.1 C) has been proposed to cause the first-cycle voltage decay. By comparing the structural evolution of $Li[Li_{0.2}Ni_{0.2}Mn_{0.6}]O_2$ (LLNMO) at various current densities, the *operando* synchrotron-based X-ray diffraction results show that the lattice strain in bulk LLNMO is continuously increased over cycling, resulting in the first-cycle voltage loss upon Li-ion insertion. Unlike the LLNMO, the accumulated average lattice strain of $LiNi_{0.8}Co_{0.1}Mn_{0.1}O_2$ (NCM811) and $LiNi_{0.6}Co_{0.2}Mn_{0.2}O_2$ (NCM622) from the open-circuit voltage to 4.8 V could be released on discharge. These findings help to gain a deep understanding of the voltage decay in LMLOs.

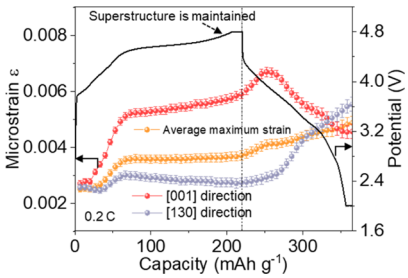

KEYWORDS: *Li-rich cathodes, voltage decay, lattice strain accumulation, layered structure, operando X-ray diffraction*

1. INTRODUCTION

Lithium-ion batteries (LIBs) have received considerable attention in the past decades because of their excellent rechargeability and high energy density.[1−4] Li- and Mn-rich layered oxide (LMLO) cathode materials are particularly attractive because they can deliver much higher specific capacities (exceeding 250 mA h g^{-1}) than the most commonly used layered Li(Ni, Co, Mn)O_2 (NCM, $R\bar{3}m$) cathode materials (around 180 mA h g^{-1}).[5−8] Such high specific capacity is attributable to the cationic and anionic redox processes in LMLOs, which are different from the transition-metal (TM) redox alone in NCM cathodes on cycling.[9−12] There is a high voltage plateau associated with the lattice oxygen oxidation in the first delithiation process, but it vanishes upon the lithiation process.[13−15] Furthermore, a continuous reduction of the average discharge voltage occurs during the subsequent cycles, which seriously restricts the commercial application of LMLOs.[16,17] These inspire tremendous research efforts to decipher the origin of the voltage decay in LMLOs.

Until now, the reasons why and how the LMLOs suffer from severe voltage decay and structural degradation with cycling have generated plenty of theories,[18−20] some of them are even conflicting. For example, the voltage decay was previously found to mainly stem from the irreversible migration of TM cations into the Li layer during cycling.[18,21,22] As more TM ions are trapped in the Li layer forming TM_{Li}-$\square_{TM}$ antisite defects ($\square$ denotes vacancy), the voltage fade is exacerbated during extended cycling. However, Bruce and co-workers[23,24] proposed that the disappearance of the honeycomb superstructure (i.e., local ordering of Li and TM ions in the TM layer), rather than the TM cation migration, is a crucial factor in the origin of first-cycle voltage decay. Very recently, Liu et al.[25] suggested that the voltage loss is controlled by the strain-induced structural degradation upon prolonged cycling. The lattice strain would progressively accumulate in the crystallites during long-term cycling, which plays a significant role in the structural degradation and the deterioration of electrochemical performance of LMLOs. This raises the crucial question of what is the key factor for the first-cycle voltage decay in the LMLO cathodes.

It is well known that the grain size and the microstrain of crystals can be indirectly determined from the analysis of the X-ray Bragg peak broadening.[26,27] As the synchrotron radiation technology has developed by leaps and bounds, acquiring hundreds of high-resolution synchrotron-based X-ray radiation diffraction (SXRD) patterns within a short time period becomes a reality.[2,28−31] In situ or *operando* high-resolution SXRD is becoming a powerful method for monitoring the changes of the lattice parameter and microstructure in the electrode materials during electrochemical cycling.[32−34] In this

study, a hydroxide coprecipitation route coupled with an annealing process was used to synthesize $Li[Li_{0.2}Ni_{0.2}Mn_{0.6}]O_2$ (LLNMO). The relationship between the microstrain and its roles in the first-cycle voltage fade of LLNMO was investigated by the *operando* high-resolution SXRD technique. For comparison, the microstructural evolution of Ni-rich layered cathode materials, i.e., $LiNi_{0.8}Co_{0.1}Mn_{0.1}O_2$ (NCM811) and $LiNi_{0.6}Co_{0.2}Mn_{0.2}O_2$ (NCM622), was also analyzed during high-voltage cycling so as to gain a broad understanding of the inherent causes of voltage fade in LLNMO.

2. RESULTS AND DISCUSSION

The pure layered LLNMO was prepared by heating hydroxide coprecipitates and Li_2CO_3; details of this synthesis process are described in the Supporting Information. The primary particle size of LLNMO is approximately 300 nm, and these grains with a platelet-like shape tend to agglomerate, forming secondary particles (Figure S1, Supporting Information). Rietveld refinement was performed by assuming a single monoclinic layered structure with space group $C2/m$, see Figure 1a, and the small residual weight percentage (R_{wp}) of

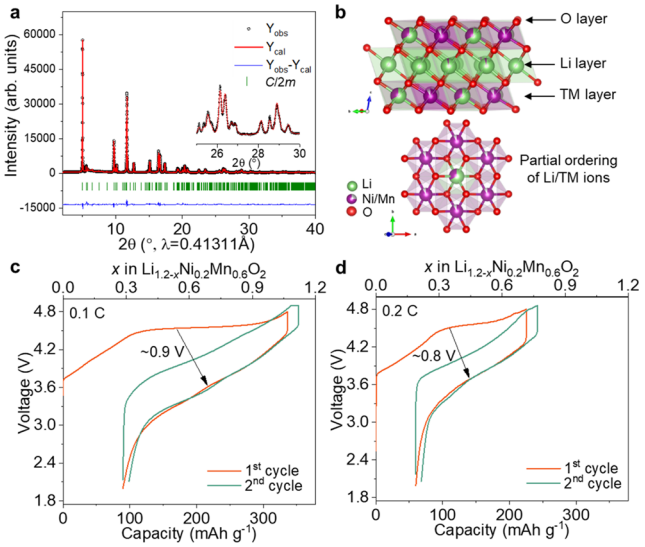

Figure 1. (a) Rietveld refinement against the SXRD pattern of LLNMO, and (b) the obtained structure model of $Li[Li_{0.2}Ni_{0.2}Mn_{0.6}]O_2$ ($C2/m$); the first two charge–discharge voltage curves of LLNMO at (c) 0.1 and (d) 0.2 C within a voltage window of 2.0–4.8 V.

4.3% suggests that the proposed the structure model is reliable (see Table S1). Figure 1b shows a partial ordering of Li and Ni/Mn ions in the TM layer in the monoclinic layered structure. To explore the correlation between the superstructure and first-cycle voltage decay, the electrochemical performances of the fabricated Li/LLNMO cells (coin-type CR2032) were tested at 25 °C between 2.0 and 4.8 V at various current densities (1 C = 320 mA g^{-1}). The initial two charge–discharge voltage profiles of LLNMO at 0.1 C are plotted in Figure 1c. The first charge profile of LLNMO displays a monotonic region below 4.5 V and a high voltage plateau at around 4.6 V, which correspond to the oxidation of Ni ions (i.e., $0.2Ni^{2+} \rightarrow 0.2Ni^{4+} + 0.4e^-$) and the oxidation of lattice oxygen ($O^{2-} \rightarrow O^{n-} + (2-n)e^-$, $0 < n < 2$),[35,36] respectively. Upon lithiation, the discharge voltage drops monotonically without an apparent voltage plateau, resulting in an obvious voltage loss (around 0.9 V). There is a smooth and monotonous charge–discharge curve in the LLNMO during the second cycle, which is comparable to that of NCM cathode materials (see below). Clearly, the LLNMO delivers similar charge–discharge characteristics at 0.2 C (Figures 1c and S2), and the high voltage plateau at 4.6 V is also visible upon the first charge. However, the discharge capacity of LLNMO at 0.2 C (173 mA h g^{-1}) is much lower than that of LLNMO at 0.1 C (246 mA h g^{-1}), revealing relatively small numbers of Li-ions participating in the redox reaction at 0.2 C. Thus, an interesting question that requires to be addressed is whether the superstructure of LLNMO is disappeared after the first cycle at 0.2 C.

Subsequently, *operando* high-resolution SXRD experiments were carried out on the Li/LLNMO cells during electrochemical cycling at a current density of 0.1 or 0.2 C. The changes in the intensity and position of several main Bragg peaks as a function of reaction time are plotted in Figure 2. When an *operando* coin cell is charged to 4.5 V at 0.1 C, the 001 and $\bar{1}33$ reflections of LLNMO gradually move to lower two-theta angles, and the 130 and $\bar{3}31$ reflections of LLNMO shift toward higher two-theta angles (Figure 2a,c). With a further increase in the charging voltage to 4.8 V, the positions of the main reflections do not change considerably, which are in good agreement with the previous results reported in the literature.[37−39] Noticeably, the 020 reflection corresponding to the honeycomb-like superstructure progressively vanishes in the voltage window of 4.5–4.8 V (see Figure 2c), hinting that the lattice oxygen oxidation is supposed to be related to the cation rearrangement in the TM layer in the monoclinic layered structure. Upon discharge, all the reflections have a tendency to move back to their initial positions. During the subsequent second charge, the changes of these reflections are almost symmetrical compared to the first discharge. In contrast, similar variations in the reflection positions are observed in the LLNMO at 0.2 C. Excitingly, the 020 reflection does not disappear completely during the first cycling, which indicates that the first-cycling voltage decay is partially independent of the evanescence of the honeycomb-like superstructure in the LLNMO cathode.

Each *operando* SXRD pattern of LLNMO during cycling was fitted using Rietveld refinement with the structure model of monoclinic layered $Li[Li_{0.2}Ni_{0.2}Mn_{0.6}]O_2$ ($C2/m$), and the resultant lattice parameters are depicted in Figure 3. As the charge voltage rises to around 4.5 V, the parameter c of LLNMO increases from 5.03(3) to 5.06(3) Å owing to an increased electrostatic repulsive force between adjacent oxygen layers.[40] Meanwhile, the parameter a decreases from 4.95(3) to 4.91(3) Å, and the parameter b reduces from 8.58(5) to 8.51(5) Å, respectively, as a result of the oxidation of Ni ions.[41] When the Li/LLNMO cell is charged to 4.8 V, around 0.85 Li ion is electrochemically extracted from $Li_{1.2}Ni_{0.2}Mn_{0.6}O_2$, corresponding to the specific capacity of ≈320 mA h g^{-1}. There are no pronounced changes in lattice parameters in the high-voltage region (4.5–4.8 V). During discharge, the parameter c increases first and then decreases successively, while the parameters of both a and b raise progressively. All lattice parameters after the first cycle are larger than their original values before cycling. The percentage changes in lattice constant of a, b, c and unit cell volume (V) of LLNMO before and after the first cycle at 0.1 C are 0.27, 0.42, 0.47, and 1.15%, respectively. Such an increase of V is caused by the irreversible Li loss from the LLNMO lattice, as evidenced by a low initial coulombic efficiency of around 75% (see Figure 1c).

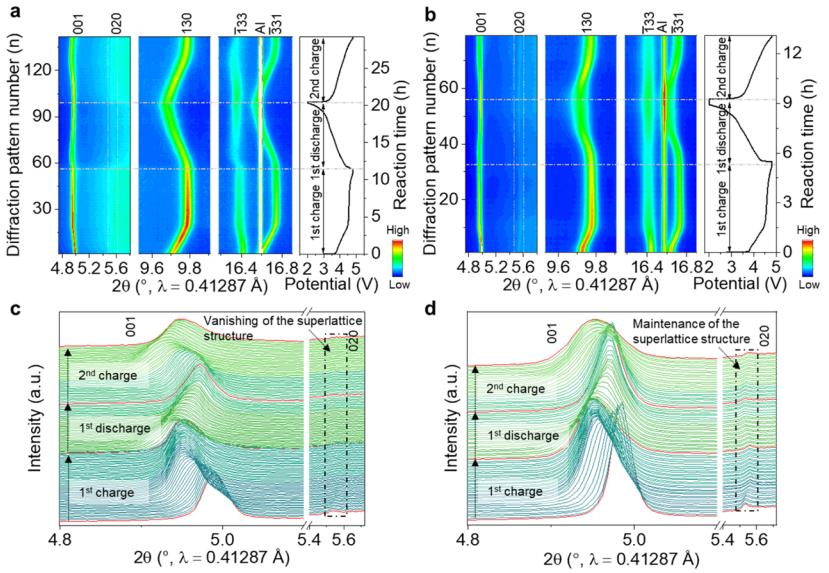

Figure 2. Contour plot of *operando* SXRD patterns of LLNMO (λ = 0.41287 Å) collected at current densities of (a) 0.1 and (b) 0.2 C, right figures display the corresponding charge–discharge voltage plots; the corresponding changes in the intensities and positions of 001 and 020 reflections at (c) 0.1 and (d) 0.2 C, showing the disappearance or maintenance of 020 superlattice reflection during cycling at 0.1 or 0.2 C.

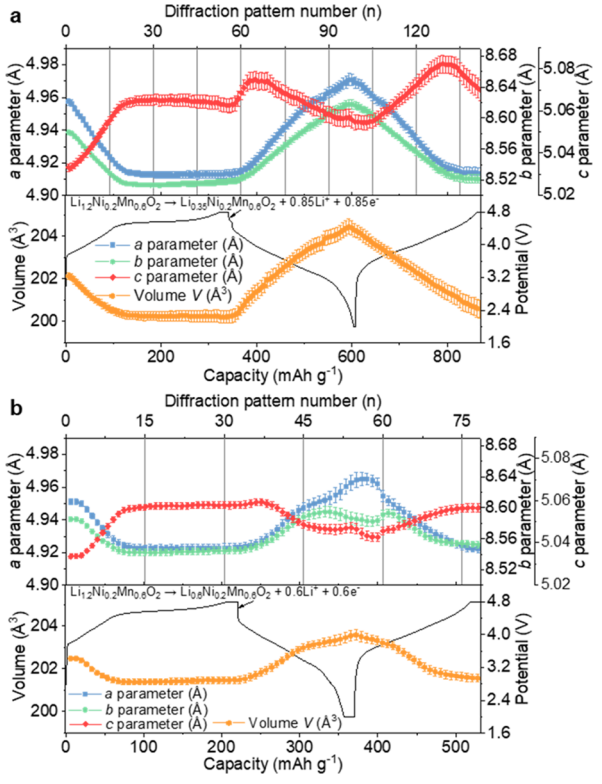

Figure 3. Variation of lattice parameters of LLNMO at (a) 0.1 and (b) 0.2 C during the first cycle and the second charge.

The increase in the *c* axis is relatively more profound than the increase in the *ab*-plane, which is supposed to be stemmed from an increased electrostatic repulsive force between the O layer and the TM layer as a consequence of the increased number of Li vacancies in LLNMO after the first cycle. Upon the second charging, the lattice parameter *c* gradually increases from 5.05(3) Å at 2.0 V to 5.08(3) Å at ≈4.3 V and then decreases to 5.07(3) Å at 4.8 V, manifesting a structural collapse in the *c*-axis in the high-voltage region (>4.5 V). Evidently, trend changes in the lattice parameters and unit-cell volume of LLNMO at 0.2 C are quite similar to those at 0.1 C, while the variation magnitudes are relatively small because of the comparably low capacity.

Operando X-ray absorption spectroscopy (XAS) experiment was performed on the Li/LLNMO cell under a current density of 0.2 C so as to investigate the changes in the oxidation state and the local structure of TM ions upon cycling, as shown in Figure 4. The Ni K-absorption edge of LLNMO moves to higher energy until the voltage reaches around 4.5 V and keeps almost unchanged from 4.5 to 4.8 V (Figure 4b), suggesting that the Ni oxidation state (Ni^{2+}) is oxidized to Ni^{4+} from open-circuit voltage to 4.5 V and remains nearly constant (i.e., Ni^{4+}) at the oxygen-involved voltage plateau, respectively. No

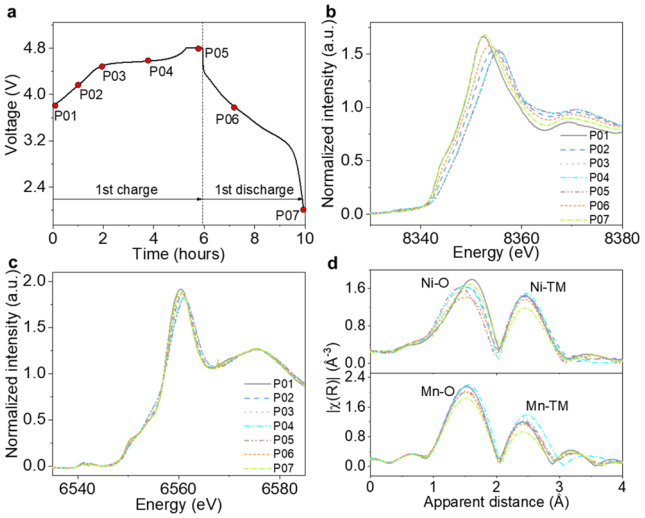

Figure 4. (a) First charge–discharge voltage curve of LLNMO during *operando* XAS experiments; normalized (b) Ni and (c) Mn K-edge XANES spectra; and (d) the corresponding Fourier transform magnitudes of k^2 weighted Ni and Mn K-edge EXAFS spectra of LLNMO upon cycling.

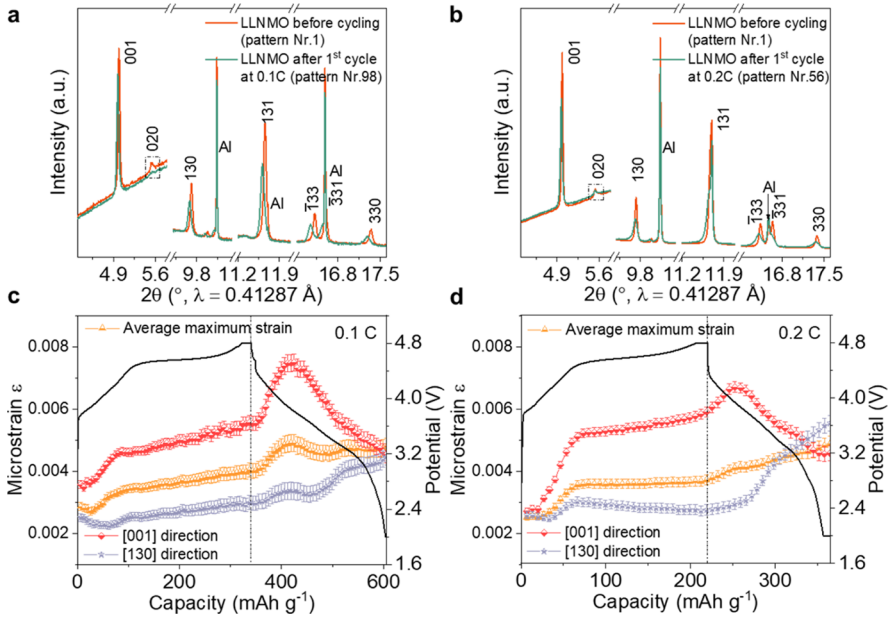

Figure 5. Comparison of SXRD patterns of LLNMO at (a) 0.1 and (b) 0.2 C before and after the first cycle; the microstrain analysis of LLNMO at (c) 0.1 and (d) 0.2 C, revealing an accumulated lattice strain as an internal trigger for voltage decay in LLNMO.

clear change in the shape and energy position of the Mn K-edge X-ray absorption near-edge structure (XANES) spectra can be observed in Figure 4c, which signifies that the Mn valence state does not vary significantly during the entire charge−discharge process. The Fourier transform (FT *R*-space) magnitudes of k^2 weighted $\chi(k)$ extended X-ray absorption fine structure (EXAFS) spectra at Mn and Ni K-edges are displayed in Figure 4d. There are two distinct peaks in the range of 1−3 Å in the FT spectra for both Ni and Mn ions, which correspond to a TM−O first coordination and a TM−TM second coordination.[42,43] Apparently, the intensities of both Ni−TM and Mn−TM peaks decline after the first cycle, revealing a relatively high degree of local structural disordering in the TM−TM interactions of cycled LLNMO.[44,45]

Although small changes of lattice parameters are involved in the LLNMO cathode during the first charge−discharge cycle at 0.2 C, the oxygen-involved voltage plateau is also disappeared during the first discharge. Therefore, it is significant to compare the *operando* SXRD patterns of LLNMO before and after the first cycle at various current densities, as illustrated in Figure 5a,b. The 020 reflection in the SXRD patterns of LLNMO is basically overlapped before and after the first cycle at 0.2 C, in sharp contrast to the disappearance of 020 reflection after the first cycle at 0.1 C. This result demonstrates that the first-cycle voltage loss is not completely controlled by the honeycomb-like bulk superstructure of LLNMO. In other words, the lattice oxygen oxidation of LLNMO at high voltage plateau (≈4.6 V) can occur without the loss of structural ordering.

Compared to the SXRD patterns of fresh LLNMO, all the reflections shift toward lower scattering angles after the first cycle, which precisely match with an expansion of unit-cell volume. Rietveld refinement results indicate that the degree of Li/TM mixing is as low as 0.03 for the LLNMO before and after the first cycle at 0.1 and 0.2 C, see Figures S3 and S4 and Table S2. The voltage decay during the first cycle cannot be solely ascribed to the migration of the TM cation into the Li layered in the layered structure. In addition, the reflection height is reduced and the reflection width is increased after the first de-intercalation/intercalation cycle. The analysis of reflection widths indicates that the grain size is larger than 100 nm, and, thus, reflection broadening appears to be dominated by the microstrain contribution.[46,47] The microstrain (ε) along the [001] direction gradually increases with initial delithiation at a current density of 0.1 C (Figure 5c), whereas the internal strain along the [130] orientation decreases. These changes agree well with the increase of lattice parameter *c* and the compression in the *ab* plane (see Figure 3a). Since the Li-ions are first extracted from the surface of LLNMO crystallites, the tensile strain takes place preferentially in the near surface region, as illustrated in Figure 6 (region I). With continuous Li-ion extraction (region II), the lattice strains along both [001] and [130] orientations gradually accumulate and propagate into the interior of the crystallites. In the beginning of discharge, the electrostatic repulsive force between O layers successively reaches its maximum (region III), probably because the oxidation state of lattice oxygen decreases with the initial discharge process. Although the lattice strain along the [001] orientation decreases with further lithiation (region IV), the tensile strain along the *ab* plane progressively accumulates, resulting in the presence of tensile average strain in the entire particle at the end of discharge. Similar variations of microstrains can be found in LLNMO at 0.2 C, as depicted in Figure 5d. Note that the lattice strain along the [130] direction slightly decreases in the high-voltage region (4.5−4.8 V), which might be correlated with maintenance of the superstructure. Very importantly, the average maximum strain of LLNMO after the first cycle, at both 0.1 and 0.2 C, is roughly two times higher than that of pristine LLNMO. Such accumulated tensile strain during the first cycle severely affects the structural stability of LLNMO and the kinetics of the interfacial Li-ion transfer process. The apparent activation energy (E_a) for the Li-ion intercalation into the LLNMO increases from 0.37 ± 0.02 eV (pristine state) to 0.47 ± 0.02 eV after the first cycle, as shown in Figures S5 and

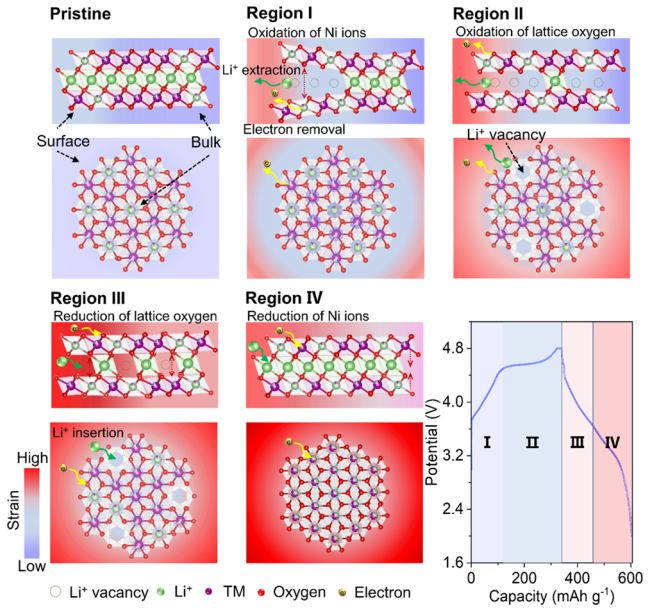

Figure 6. Schematic illustration of the correlation between strain accumulation and structural evolution of LLNMO during the first cycle.

S6 and Table S3. Therefore, these results reveal that, as long as the oxidation of lattice oxygen is involved during the initial charge, an accumulated lattice strain over cycling could trigger the voltage fading in LLNMO.[25]

It is well acknowledged that the conventional NCM cathode materials do not show the pronounced voltage decay during the first cycle, even at high-voltage operation.[48,49] Exploration of the microstructural evolution of Ni-rich cathode materials upon the first cycle, therefore, is particularly interesting. The layered NCM811 with quasi-spherical-shaped agglomerates was also prepared by a hydroxide co-precipitation method followed by a high-temperature solid-state reaction (Figures S7 and S8 and Table S4). Figure 7a exhibits the initial charge–discharge voltage curves of the NCM811 at a current density of 28 mA g^{-1} (0.1 C) between 2.7 and 4.8 V. The NCM811 possesses a monotonically increasing charge profile with a specific capacity of 262 mA h g^{-1} and a monotonically decreasing discharge plot with a specific capacity of 236 mA h g^{-1}. The continuous changes of the position and height of reflections in the *operando* SXRD patterns of NCM811 during cycling suggest a typical solid–solution reaction (Figure 7c), which is in good agreement with the monotonous charge–discharge profiles in the voltage range of 2.7–4.8 V. Very interestingly, only subtle variations in the reflection positions are observed in NCM811 after the first cycle (Figure 7b), and full width at half-maximum (fwhm) of reflections does not increase clearly. Figure 7d shows the lattice parameters derived from the *operando* SXRD patterns of NCM811 upon cycling (Figure S9). The lattice parameter *c* of NCM811 increases gradually in the range from open-circuit voltage to about 4.2 V and then drops significantly with the potential increasing to 4.8 V. The parameter *a* of NCM811 progressively decreases from OCV to 4.8 V. The results agree well with the previous analysis of in situ XRD patterns of NCM811.[50,51] NCM811 experiences a gradual accumulation of tensile strain along the [003] direction upon charge. The lattice strain along the [101] direction first increases when the voltage profile reaching about 4.2 V, and drops substantially as the potential further increases to 4.8 V. What is worth noticing is that the lattice strain evolution during high-voltage cycling is highly reversible.

To gain a general understanding of the structural degradation of Ni-rich layered cathode materials, the NCM622 was also synthesized (see Figures S10 and S11 and Table S6). Evidently, there is also no high-voltage plateau at about 4.6 V in NCM622 during the first lithium extraction process (Figure S12). The charge–discharge voltage profiles and the *operando* SXRD patterns of NCM622 are shown in Figure S13. The changes in lattice parameters and microstrain of NCM622 between 2.7 and 4.8 V are very similar to those of NMC811 (Figures S14–S16 and Table S7). Very significantly, the average maximum strain of both NCM622 and NCM811

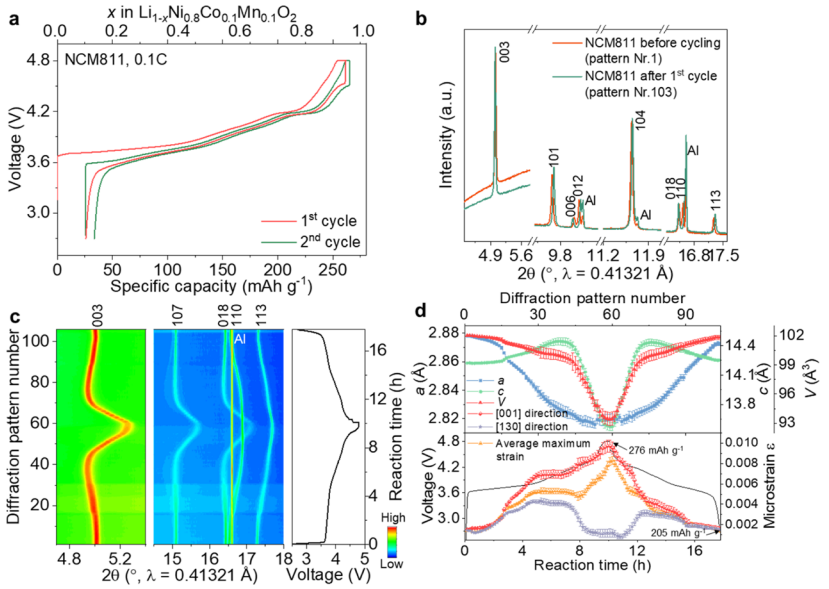

Figure 7. (a) Charge–discharge voltage profiles of NCM811 during the first and second cycles; (b) contour plot of *operando* SXRD patterns of NCM811 (λ = 0.41321 Å) during the first cycle; (c) a comparison of SXRD patterns of NCM811 before and after the first cycle within an *operando* cell; (d) variations of lattice parameters and microstructural strain of NCM811 upon cycling.

at 4.8 V (≈0.008) is higher than that of LLNMO at 4.8 V (≈0.004), but these values of NCM622 and NCM811 reduce to ≈0.002 after one cycle in sharp contrast to that of LLNMO (≈0.005). These data imply that, although the Ni-rich cathode materials suffer from a large accumulation of average lattice strain upon charge, the accumulating strain is released upon discharge. The activation energy for the Li-ion inserted into the NCM811 or NCM622 does not increase pronouncedly after the first cycle (see Figures S5 and S6 and Table S3). By contrast, the apparent activation energy of LLNMO increases with the accumulation of average lattice strain upon cycling. Such strain-induced structural degradation is supposed to be the main cause for the severe voltage decay in LLNMO during the first cycle.

3. CONCLUSIONS

In summary, the structural evolution of monoclinic layered LLNMO ($C2/m$) during the first cycle was carefully investigated by *operando* SXRD and XAS techniques. Unlike the vanishing of a partial ordering of Li and TM cations in the layered structure upon the first charge at 0.1 C, the honeycomb-like bulk superstructure of LLNMO is well maintained after the first cycle at 0.2 C. The experimental results demonstrate that the first-cycle voltage decay of LLNMO cannot be solely attributed to the superstructure and/or the cation migration. Instead, the lattice strain is adversely accumulated inside the crystals in the first cycle, which is found to be an intrinsic trigger for the voltage fade in LLNMO. By contrast, although a pronounced increase in the average lattice strain is detected in NCM811 and NCM622 during high-voltage cycling (2.7−4.8 V), the accumulated lattice strain would be released on discharge. Accordingly, a necessary prerequisite for mitigating the voltage decay in LMLOs is to promote the release of the accumulated strain upon electrochemical cycling. These findings provide new insights into the origin of voltage loss in LMLOs and important clues to improve the electrochemical performance of advanced LIBs.

AUTHOR INFORMATION

Corresponding Author

Weibo Hua − *School of Chemical Engineering and Technology, Xi'an Jiaotong University, Xi'an, Shaanxi 710049, China; School of Chemical Engineering, Sichuan University, 610065 Chengdu, China; Institute for Applied Materials (IAM), Karlsruhe Institute of Technology (KIT), D-76344 Eggenstein-Leopoldshafen, Germany; Key Laboratory of Advanced Energy Materials Chemistry (Ministry of Education), College of Chemistry, Nankai University, Tianjin 300071, China;* orcid.org/0000-0001-5372-4422; Email: weibo.hua@xjtu.edu.cn

Authors

Suning Wang − *School of Chemical Engineering and Technology, Xi'an Jiaotong University, Xi'an, Shaanxi 710049, China; Institute for Applied Materials (IAM), Karlsruhe Institute of Technology (KIT), D-76344 Eggenstein-Leopoldshafen, Germany; College of Materials Science and Engineering, Guilin University of Technology, Guilin 541004, China;* orcid.org/0000-0001-8910-9069

Tian Zhao − *School of Chemical Engineering and Technology, Xi'an Jiaotong University, Xi'an, Shaanxi 710049, China*

Jinniu Chen − *School of Chemical Engineering and Technology, Xi'an Jiaotong University, Xi'an, Shaanxi 710049, China*

Alexander Missyul − *CELLS-ALBA Synchrotron, Barcelona E-08290, Spain;* orcid.org/0000-0002-0577-4481

Laura Simonelli − *CELLS-ALBA Synchrotron, Barcelona E-08290, Spain;* orcid.org/0000-0001-5331-0633

Laijun Liu − *College of Materials Science and Engineering, Guilin University of Technology, Guilin 541004, China;* orcid.org/0000-0002-6889-2506

Fujun Li − *Key Laboratory of Advanced Energy Materials Chemistry (Ministry of Education), College of Chemistry, Nankai University, Tianjin 300071, China;* orcid.org/0000-0002-1298-0267

Xiangyang Kong − *School of Materials Science and Engineering, Shanghai Jiao Tong University, Shanghai 200240, China*

Author Contributions

△ S.W. and T.Z. contributed equally to this work. W.H. conceived the idea and discussed with S.W., A.M., L.L., F.L., and X.K.; S.W., T.Z., Z.J., and J.C. carried out the preparation experiments; W.H., A.M., and L.S. performed the synchrotron-based X-ray diffraction and absorption measurements; the data were analyzed by S.W., T.Z., and W.H.; W.H. and S.W. wrote the preliminary draft with input L.L., F.L., and X.K.; all authors revised the manuscript and have given the approval to the final version of the manuscript.

Notes

The authors declare no competing financial interest.

ACKNOWLEDGMENTS

This work was financially supported by the National Natural Science Foundation of China (grant no. 22108218), the Guangxi Science and Technology Base and Talents Special Project (grant no. AD21159007), and the Natural Science Foundation of Guangxi (grant no. 2020GXNSFBA297029). W.H. acknowledges "Young Talent Support Plan" of Xi'an Jiaotong University (71211201010723) and Qinchuangyuan Innovative Talent Project (QCYRCXM-2022-137). Our research work gained benefit from beamtime allocation at BL04-MSPD at ALBA Synchrotron (proposal number: 2017032159, 2017092393, 2018022669, and 2020094655), Barcelona, Spain. The authors gratefully acknowledge Zhiwei Jing for helping with the sample synthesis. We also thank the Instrument Analysis Center of Xi'an Jiaotong University for the assistance test. This work contributes to the research performed at CELEST (Center for Electrochemical Energy Storage Ulm-Karlsruhe) and was supported by the German

Research Foundation (DFG) under Project ID 390874152 (POLiS Cluster of Excellence).

REFERENCES

(1) Lun, Z.; Ouyang, B.; Kwon, D. H.; Ha, Y.; Foley, E. E.; Huang, T. Y.; Cai, Z.; Kim, H.; Balasubramanian, M.; Sun, Y.; Huang, J.; Tian, Y.; Kim, H.; McCloskey, B. D.; Yang, W.; Clement, R. J.; Ji, H.; Ceder, G. *Nat. Mater.* **2021**, *20*, 214−221.

(2) Xu, C.; Marker, K.; Lee, J.; Mahadevegowda, A.; Reeves, P. J.; Day, S. J.; Groh, M. F.; Emge, S. P.; Ducati, C.; Layla Mehdi, B.; Tang, C. C.; Grey, C. P. *Nat. Mater.* **2021**, *20*, 84−92.

(3) Wang, L. G.; Liu, T. C.; Wu, T. P.; Lu, J. *Nature* **2022**, *611*, 61−67.

(4) Xiao, Y.; Wang, H. R.; Hu, H. Y.; Zhu, Y. F.; Li, S.; Li, J. Y.; Wu, X. W.; Chou, S. L. *Adv. Mater.* **2022**, *34*, 2202695.

(5) Hua, W.; Yang, X.; Casati, N. P. M.; Liu, L.; Wang, S.; Baran, V.; Knapp, M.; Ehrenberg, H.; Indris, S. *eScience* **2022**, *2*, 183−191.

(6) He, W.; Guo, W.; Wu, H.; Lin, L.; Liu, Q.; Han, X.; Xie, Q.; Liu, P.; Zheng, H.; Wang, L.; Yu, X.; Peng, D. L. *Adv. Mater.* **2021**, *33*, 2005937.

(7) Liu, H.; Zhao, C.; Qiu, Q.; Hu, B.; Geng, F.; Li, J.; Tong, W.; Hu, B.; Li, C. *J. Phys. Chem. Lett.* **2021**, *12*, 8740−8748.

(8) Hu, H. Y.; Zhu, Y. F.; Xiao, Y.; Li, S.; Li, J. Y.; Hao, Z. Q.; Zhao, J. H.; Chou, S. L. *Adv. Energy Mater.* **2022**, *12*, 2201511.

(9) Wang, S.; Hua, W.; Missyul, A.; Darma, M. S. D.; Tayal, A.; Indris, S.; Ehrenberg, H.; Liu, L.; Knapp, M. *Adv. Funct. Mater.* **2021**, *31*, 2009949.

(10) Hua, W.; Chen, M.; Schwarz, B.; Knapp, M.; Bruns, M.; Barthel, J.; Yang, X.; Sigel, F.; Azmi, R.; Senyshyn, A.; Missiul, A.; Simonelli, L.; Etter, M.; Wang, S.; Mu, X.; Fiedler, A.; Binder, J. R.; Guo, X.; Chou, S.; Zhong, B.; Indris, S.; Ehrenberg, H. *Adv. Energy Mater.* **2019**, *9*, 1803094.

(11) Grenier, A.; Kamm, G. E.; Li, Y.; Chung, H.; Meng, Y. S.; Chapman, K. W. *J. Am. Chem. Soc.* **2021**, *143*, 5763−5770.

(12) Li, J.; Hu, H.; Wang, J.; Xiao, Y. *Carbon Neutralization* **2022**, *1*, 96−116.

(13) He, J. R.; Hua, W. B.; Missiul, A.; Melinte, G.; Das, C.; Tayal, A.; Bergfeldt, T.; Mangold, S.; Liu, X. Y.; Binder, J. R.; Knapp, M.; Ehrenberg, H.; Indris, S.; Schwarz, B.; Maibach, J. *J. Mater. Chem. A* **2021**, *9*, 264−273.

(14) Zuo, W.; Luo, M.; Liu, X.; Wu, J.; Liu, H.; Li, J.; Winter, M.; Fu, R.; Yang, W.; Yang, Y. *Energy Environ. Sci.* **2020**, *13*, 4450−4497.

(15) Qiu, L.; Zhang, M.; Song, Y.; Wu, Z.; Zhu, Y. F.; Zhang, J.; Wang, D.; Hu, H. Y.; Li, H. W.; Liu, H. R.; Jia, X. B.; Peng, J.; Chen, S.; Yang, Z.; Xiao, Y.; Guo, X. *Carbon Energy* **2022**, DOI: 10.1002/cey2.298.

(16) Zhang, J.; Zhang, Q.; Wong, D.; Zhang, N.; Ren, G.; Gu, L.; Schulz, C.; He, L.; Yu, Y.; Liu, X. *Nat. Commun.* **2021**, *12*, 3071.

(17) Saha, S.; Assat, G.; Sougrati, M. T.; Foix, D.; Li, H.; Vergnet, J.; Turi, S.; Ha, Y.; Yang, W.; Cabana, J.; Rousse, G.; Abakumov, A. M.; Tarascon, J.-M. *Nat. Energy* **2019**, *4*, 977−987.

(18) Eum, D.; Kim, B.; Kim, S. J.; Park, H.; Wu, J.; Cho, S. P.; Yoon, G.; Lee, M. H.; Jung, S. K.; Yang, W.; Seong, W. M.; Ku, K.; Tamwattana, O.; Park, S. K.; Hwang, I.; Kang, K. *Nat. Mater.* **2020**, *19*, 419−427.

(19) Sathiya, M.; Abakumov, A. M.; Foix, D.; Rousse, G.; Ramesha, K.; Saubanere, M.; Doublet, M. L.; Vezin, H.; Laisa, C. P.; Prakash, A. S.; Gonbeau, D.; VanTendeloo, G.; Tarascon, J. M. *Nat. Mater.* **2015**, *14*, 230−238.

(20) Zhang, J.; Wang, Q. C.; Li, S. F.; Jiang, Z. S.; Tan, S.; Wang, X. L.; Zhang, K.; Yuan, Q. X.; Lee, S. J.; Titus, C. J.; Irwin, K. D.; Nordlund, D.; Lee, J. S.; Pianetta, P.; Yu, X. Q.; Xiao, X. H.; Yang, X. Q.; Hu, E. Y.; Liu, Y. J. *Nat. Commun.* **2020**, *11*, 6342.

(21) Mohanty, D.; Li, J.; Abraham, D. P.; Huq, A.; Payzant, E. A.; Wood, D. L.; Daniel, C. *Chem. Mater.* **2014**, *26*, 6272−6280.

(22) Zheng, J. M.; Myeong, S. J.; Cho, W. R.; Yan, P. F.; Xiao, J.; Wang, C. M.; Cho, J.; Zhang, J. G. *Adv. Energy Mater.* **2017**, *7*, 1601284.

(23) House, R. A.; Maitra, U.; Perez-Osorio, M. A.; Lozano, J. G.; Jin, L.; Somerville, J. W.; Duda, L. C.; Nag, A.; Walters, A.; Zhou, K. J.; Roberts, M. R.; Bruce, P. G. *Nature* **2020**, *577*, 502−508.

(24) House, R. A.; Rees, G. J.; Pérez-Osorio, M. A.; Marie, J.-J.; Boivin, E.; Robertson, A. W.; Nag, A.; Garcia-Fernandez, M.; Zhou, K.-J.; Bruce, P. G. *Nat. Energy* **2020**, *5*, 777−785.

(25) Liu, T. C.; Liu, J. J.; Li, L. X.; Yu, L.; Diao, J. C.; Zhou, T.; Li, S. N.; Dai, A.; Zhao, W. G.; Xu, S. Y.; Ren, Y.; Wang, L. G.; Wu, T. P.; Qi, R.; Xiao, Y. G.; Zheng, J. X.; Cha, W.; Harder, R.; Robinson, I.; Wen, J. G.; Lu, J.; Pan, F.; Amine, K. *Nature* **2022**, *606*, 305−312.

(26) Borbely, A.; Groma, I. *Appl. Phys. Lett.* **2001**, *79*, 1772−1774.

(27) Li, S.; Qian, G.; He, X.; Huang, X.; Lee, S. J.; Jiang, Z.; Yang, Y.; Wang, W. N.; Meng, D.; Yu, C.; Lee, J. S.; Chu, Y. S.; Ma, Z. F.; Pianetta, P.; Qiu, J.; Li, L.; Zhao, K.; Liu, Y. *Nat. Commun.* **2022**, *13*, 704.

(28) Chen, J.; Yang, Y.; Tang, Y.; Wang, Y.; Li, H.; Xiao, X.; Wang, S.; Darma, M. S. D.; Etter, M.; Missyul, A.; Tayal, A.; Knapp, M.; Ehrenberg, H.; Indris, S.; Hua, W. *Adv. Funct. Mater.* **2022**, *33*, 2211515.

(29) Wang, S.; Hua, W.; Zhou, S.; He, X.; Liu, L. *Chem. Eng. J.* **2020**, *400*, 125998.

(30) Tan, S.; Shadike, Z.; Li, J.; Wang, X.; Yang, Y.; Lin, R.; Cresce, A.; Hu, J.; Hunt, A.; Waluyo, I.; Ma, L.; Monaco, F.; Cloetens, P.; Xiao, J.; Liu, Y.; Yang, X.-Q.; Xu, K.; Hu, E. *Nat. Energy* **2022**, *7*, 484−494.

(31) Wu, C.; Qiu, L.; Wang, D. Q.; Chen, T.; Li, J.; Wu, Z. G.; Song, Y.; Guo, X. D. *Ind. Eng. Chem. Res.* **2022**, *61*, 453−463.

(32) Hua, W. B.; Schwarz, B.; Azmi, R.; Muller, M.; Dewi Darma, M. S.; Knapp, M.; Senyshyn, A.; Heere, M.; Missyul, A.; Simonelli, L.; Binder, J. R.; Indris, S.; Ehrenberg, H. *Nano Energy* **2020**, *78*, 105231.

(33) Xiao, B.; Liu, X.; Chen, X.; Lee, G. H.; Song, M.; Yang, X.; Omenya, F.; Reed, D. M.; Sprenkle, V.; Ren, Y.; Sun, C. J.; Yang, W.; Amine, K.; Li, X.; Xu, G.; Li, X. *Adv. Mater.* **2021**, *33*, 2107141.

(34) Qiu, L.; Song, Y.; Zhang, M. K.; Liu, Y. H.; Yang, Z. W.; Wu, Z. G.; Zhang, H.; Xiang, W.; Liu, Y. X.; Wang, G. K.; Sun, Y.; Zhang, J.; Zhang, B.; Guo, X. D. *Adv. Energy Mater.* **2022**, *12*, 2200022.

(35) Hua, W. B.; Wang, S. N.; Knapp, M.; Leake, S. J.; Senyshyn, A.; Richter, C.; Yavuz, M.; Binder, J. R.; Grey, C. P.; Ehrenberg, H.; Indris, S.; Schwarz, B. *Nat. Commun.* **2019**, *10*, 5365.

(36) Ding, X.; Luo, D.; Cui, J.; Xie, H.; Ren, Q.; Lin, Z. *Angew. Chem., Int. Ed.* **2020**, *59*, 7778−7782.

(37) Cui, C.; Fan, X.; Zhou, X.; Chen, J.; Wang, Q.; Ma, L.; Yang, C.; Hu, E.; Yang, X. Q.; Wang, C. *J. Am. Chem. Soc.* **2020**, *142*, 8918−8927.

(38) Li, S.; Lee, S. J.; Wang, X.; Yang, W.; Huang, H.; Swetz, D. S.; Doriese, W. B.; O'Neil, G. C.; Ullom, J. N.; Titus, C. J.; Irwin, K. D.; Lee, H. K.; Nordlund, D.; Pianetta, P.; Yu, C.; Qiu, J.; Yu, X.; Yang, X. Q.; Hu, E.; Lee, J. S.; Liu, Y. *J. Am. Chem. Soc.* **2019**, *141*, 12079−12086.

(39) Li, X.; Qiao, Y.; Guo, S.; Xu, Z.; Zhu, H.; Zhang, X.; Yuan, Y.; He, P.; Ishida, M.; Zhou, H. *Adv. Mater.* **2018**, *30*, No. e1705197.

(40) Yin, W.; Grimaud, A.; Rousse, G.; Abakumov, A. M.; Senyshyn, A.; Zhang, L.; Trabesinger, S.; Iadecola, A.; Foix, D.; Giaume, D.; Tarascon, J. M. *Nat. Commun.* **2020**, *11*, 1252.

(41) Wu, T.; Liu, X.; Zhang, X.; Lu, Y.; Wang, B.; Deng, Q.; Yang, Y.; Wang, E.; Lyu, Z.; Li, Y.; Wang, Y.; Lyu, Y.; He, C.; Ren, Y.; Xu, G.; Sun, X.; Amine, K.; Yu, H. *Adv. Mater.* **2021**, *33*, 2001358.

(42) Yang, X.; Wang, S.; Han, D.; Wang, K.; Tayal, A.; Baran, V.; Missyul, A.; Fu, Q.; Song, J.; Ehrenberg, H.; Indris, S.; Hua, W. *Small* **2022**, *18*, 2201522.

(43) Cheng, Z.; Fan, X. Y.; Yu, L.; Hua, W.; Guo, Y. J.; Feng, Y. H.; Ji, F. D.; Liu, M.; Yin, Y. X.; Han, X.; Guo, Y. G.; Wang, P. F. *Angew. Chem., Int. Ed.* **2022**, *61*, No. e202117728.

(44) Yu, X.; Lyu, Y.; Gu, L.; Wu, H.; Bak, S.-M.; Zhou, Y.; Amine, K.; Ehrlich, S. N.; Li, H.; Nam, K.-W.; Yang, X.-Q. *Adv. Energy Mater.* **2014**, *4*, 1300950.

(45) Hua, W.; Zhang, J.; Wang, S.; Cheng, Y.; Li, H.; Tseng, J.; Wu, Z.; Shen, C. H.; Dolotko, O.; Liu, H.; Hung, S. F.; Tang, W.; Li, M.;

Knapp, M.; Ehrenberg, H.; Indris, S.; Guo, X. *Angew. Chem., Int. Ed.* **2023**, *62*, No. e202214880.
(46) Zapata Dominguez, D.; Berhaut, C. L.; Buzlukov, A.; Bardet, M.; Kumar, P.; Jouneau, P. H.; Desrues, A.; Soloy, A.; Haon, C.; Herlin-Boime, N.; Tardif, S.; Lyonnard, S.; Pouget, S. *ACS Nano* **2022**, *16*, 9819−9829.
(47) Leineweber, A. *Z. Kristallogr.* **2011**, *226*, 905−923.
(48) Maleki Kheimeh Sari, H.; Li, X. F. *Adv. Energy Mater.* **2019**, *9*, 1901597.
(49) Wang, L.; Lei, X.; Liu, T.; Dai, A.; Su, D.; Amine, K.; Lu, J.; Wu, T. *Adv. Mater.* **2022**, *34*, No. e2200744.
(50) Yang, J.; Xia, Y. *ACS Appl. Mater. Interfaces* **2016**, *8*, 1297−1308.
(51) Choi, J. U.; Voronina, N.; Sun, Y. K.; Myung, S. T. *Adv. Energy Mater.* **2020**, *10*, 2002027.